A&A 563, A94 (2014)
DOI: 10.1051/0004-6361/201323288

Astronomy & Astrophysics

The *Gaia*-ESO Survey: Kinematic structure in the Gamma Velorum cluster⋆,⋆⋆

R. D. Jeffries[1], R. J. Jackson[1], M. Cottaar[2], S. E. Koposov[3], A. C. Lanzafame[4], M. R. Meyer[2], L. Prisinzano[5], S. Randich[6], G. G. Sacco[6], E. Brugaletta[4], M. Caramazza[5], F. Damiani[5], E. Franciosini[6], A. Frasca[7], G. Gilmore[3], S. Feltzing[9], G. Micela[5], E. Alfaro[8], T. Bensby[9], E. Pancino[10], A. Recio-Blanco[11], P. de Laverny[11], J. Lewis[3], L. Magrini[6], L. Morbidelli[6], M. T. Costado[8], P. Jofré[3], A. Klutsch[7], K. Lind[3], and E. Maiorca[6]

[1] Astrophysics Group, Keele University, Keele ST5 5BG, UK
e-mail: r.d.jeffries@keele.ac.uk
[2] Institute for Astronomy, ETH Zurich, Wolfgang-Pauli-Strasse 27, 8093 Zurich, Switzerland
[3] Institute of Astronomy, University of Cambridge, Madingley Road, Cambridge CB3 0HA, UK
[4] Dipartimento di Fisica e Astronomia, Sezione Astrofisica, Università di Catania, via S. Sofia 78, 95123 Catania, Italy
[5] INAF – Osservatorio Astronomico di Palermo, Piazza del Parlamento 1, 90134 Palermo, Italy
[6] INAF – Osservatorio Astrofisico di Arcetri, Largo E. Fermi 5, 50125 Florence, Italy
[7] INAF – Osservatorio Astrofisico di Catania, via S. Sofia 78, 95123 Catania, Italy
[8] Instituto de Astrofísica de Andalucía-CSIC, Apdo. 3004, 18080 Granada, Spain
[9] Lund Observatory, Department of Astronomy and Theoretical Physics, Box 43, 221 00 Lund, Sweden
[10] INAF – Osservatorio Astronomico di Bologna, via Ranzani 1, 40127 Bologna, Italy
[11] Laboratoire Lagrange (UMR7293), Université de Nice Sophia Antipolis, CNRS, Observatoire de la Côte d'Azur, BP 4229, 06304 Nice Cedex 4, France

Received 18 December 2013 / Accepted 20 January 2014

ABSTRACT

Context. A key science goal of the *Gaia*-ESO survey (GES) at the VLT is to use the kinematics of low-mass stars in young clusters and star forming regions to probe their dynamical histories and how they populate the field as they become unbound. The clustering of low-mass stars around the massive Wolf-Rayet binary system γ^2 Velorum was one of the first GES targets.
Aims. We empirically determine the radial velocity precision of GES data, construct a kinematically unbiased sample of cluster members and characterise their dynamical state.
Methods. Targets were selected from colour–magnitude diagrams and intermediate resolution spectroscopy was used to derive radial velocities and assess membership from the strength of the Li I 6708 Å line. The radial velocity distribution was analysed using a maximum likelihood technique that accounts for unresolved binaries.
Results. The GES radial velocity precision is about 0.25 km s^{-1} and sufficient to resolve velocity structure in the low-mass population around γ^2 Vel. The structure is well fitted by two kinematic components with roughly equal numbers of stars; the first has an intrinsic dispersion of 0.34 ± 0.16 km s^{-1}, consistent with virial equilibrium. The second has a broader dispersion of 1.60 ± 0.37 km s^{-1} and is offset from the first by $\simeq$2 km s^{-1}. The first population is older by 1–2 Myr based on a greater level of Li depletion seen among its M-type stars and is probably more centrally concentrated around γ^2 Vel.
Conclusions. We consider several formation scenarios, concluding that the two kinematic components are a bound remnant of the original, denser cluster that formed γ^2 Vel, and a dispersed population from the wider Vela OB2 association, of which γ^2 Vel is the most massive member. The apparent youth of γ^2 Vel compared to the older ($\geq$10 Myr) low-mass population surrounding it suggests a scenario in which the massive binary formed in a clustered environment after the formation of the bulk of the low-mass stars.

Key words. stars: pre-main sequence – stars: kinematics and dynamics – open clusters and associations: individual: gamma2 Velorum – stars: formation

1. Introduction

The *Gaia*-ESO survey (GES) is employing the FLAMES multi-object spectrograph (Pasquini et al. 2002) on the VLT UT-2 (Kueyen) telescope to obtain high quality, uniformly calibrated spectroscopy of $>10^5$ stars in the Milky Way (Gilmore et al. 2012; Randich & Gilmore 2013). The survey covers stars in the halo, bulge, thick and thin discs, as well as in star forming regions and clusters of all ages. Samples are chosen from photometric surveys with the overarching aim of characterizing the chemical and kinematic evolution of these populations. The survey will provide a rich dataset which, when combined with proper motions and parallaxes from the forthcoming *Gaia* mission (Perryman et al. 2001), will simultaneously yield 3D spatial distributions, 3D kinematics, chemical abundances and astrophysical parameters for large numbers of representative stars.

One of the key science drivers of the survey is probing the formation and subsequent dissolution of young clusters and associations using the kinematics of their constituent low-mass

⋆ Based on observations collected with the FLAMES spectrograph at VLT/UT2 telescope (Paranal Observatory, ESO, Chile), for the *Gaia*-ESO Large Public Survey (188.B-3002).
⋆⋆ Full Table 2 is only available at the CDS via anonymous ftp to cdsarc.u-strasbg.fr (130.79.128.5) or via http://cdsarc.u-strasbg.fr/viz-bin/qcat?J/A+A/563/A94

stars. It is often claimed that most stars form in clusters, but a comparison of the observed number of clusters embedded in their natal gas with older, gas-free open clusters suggests that 90 per cent of clusters must either start in an unbound state or become unbound during this transition (Carpenter 2000; Lada & Lada 2003). The heating and subsequent expulsion of gas by ionising radiation, winds or supernovae in clusters containing high-mass stars, but with relatively low star forming efficiency, is likely to unbind a significant fraction of their stars and possibly disrupt the whole cluster (Tutukov 1978; Hills 1980; Goodwin & Bastian 2006; Baumgardt & Kroupa 2007; Bastian 2011). OB associations have a similar stellar content to young clusters but are of much lower density and may be the unbound remnants or halos of clusters after the gas expulsion phase (Kroupa et al. 2001; Clark et al. 2005). Alternatively, it is possible that the importance of clustered star formation has been overestimated and that stars are formed hierarchically in environments with a wide range of initial densities; bound clusters are formed from the densest regions whilst associations formed at low densities and were possibly never bound to begin with (e.g. Bressert et al. 2010; Bonnell et al. 2011; Kruijssen et al. 2012).

The key to understanding the past and future evolution of clusters and associations lies in careful measurements of the positions and velocities of their constituent stars. *Gaia* will ultimately yield very precise tangential motions, but observations of radial velocities (RVs) and RV distributions in cluster and association populations can be used to assess membership, probe the current dynamical state, search for and parametrise binary populations, and investigate spatially coherent velocity gradients or substructure that might give clues to the initial conditions or reveal multiple populations (e.g. Jeffries et al. 2006; Fűrész et al. 2006, 2008; Briceño et al. 2007; Sacco et al. 2008; Maxted et al. 2008; Tobin et al. 2009; Cottaar et al. 2012a).

The GES began on 31 December 2011 and will be completed over the course of ≃5 years. Many important results regarding the issues discussed above will emerge from a homogeneous analysis of the ≃30 young (<1 Gyr) clusters that will eventually be targeted, but significant progress can be made before then because the data for individual clusters are usually collected in one observing season, and these datasets can serve to refine and test analysis techniques. The first "cluster" target was the collection of young, low-mass stars around the massive WC8/O8III binary system, γ^2 Velorum (HD 68273, WR11; Smith 1968; Schaerer et al. 1997). This binary, with a 78.5-day period and eccentricity of 0.33 (North et al. 2007), is the most massive member of the common proper motion Vela OB2 association, consisting of 93 early-type candidate members spread over 100 square degrees (de Zeeuw et al. 1999). The Wolf-Rayet and O-star components have current masses of 9 $M_\odot$ + 30 $M_\odot$ (de Marco & Schmutz 1999), but initial masses of about 35 $M_\odot$ + 31.5 $M_\odot$ (Eldridge 2009). A further common proper motion component of the system, γ^1 Vel (HD 68243), is separated by 41 arcsecs to the south-west and is itself a multiple system containing a close SB1 binary with a B2III primary (Hernández & Sahade 1980) and a tertiary at 0.037 arcsecs that is 1.8 mag fainter (Tokovinin et al. 2010). A surrounding association of low-mass pre-main-sequence (PMS) stars was first identified by Pozzo et al. (2000) by virtue of their strong X-ray emission. A consideration of the colour-magnitude diagram of the X-ray sources and their concentration around γ^2 Vel, led Pozzo et al. to conclude that the PMS stars were coeval with the massive binary at an age of ∼4 Myr, and at a distance of 350–400 pc. This distance is approximately consistent with the revised HIPPARCOS parallax-based distance to γ^2 Vel of 334^{+40}_{-32} pc (van Leeuwen 2007) and with interferometric determinations of 368^{+38}_{-13} pc and 336^{+8}_{-7} pc by Millour et al. (2007) and North et al. (2007) respectively.

Jeffries et al. (2009, hereafter J09) made a further study of the relationship between γ^2 Vel, Vela OB2 and the X-ray-active PMS stars using a 0.9 square degree *BVI* photometric survey centred on γ^2 Vel, supported by *XMM-Newton* X-ray observations and some fibre spectroscopy of solar-type candidate association members. They confirmed that the PMS stars are strong X-ray emitters and are spatially concentrated around γ^2 Vel. The PMS stars also have proper motions and RVs consistent with γ^2 Vel and Vela OB2, and main-sequence fitting to stars in the wider Vela OB2 association gives a distance that coincides with the distance to γ^2 Vel and the main-sequence fitting distance to the early-type stars immediately surrounding it. Using PMS isochrones and a handful of observations of lithium in K-type kinematic members, J09 claimed an age of 5–10 Myr for the low-mass PMS stars. A *Spitzer* survey for circumstellar material around the low-mass association members reported by Hernández et al. (2008) revealed a very low disc frequency that may be consistent with this age estimate given the short disc half-life of ≃3 Myr found from *Spitzer* observations of many other young clusters. On the basis of a 3–4 Myr age estimate for γ^2 Vel made by de Marco & Schmutz (1999) and North et al. (2007), J09 suggested a cluster formation scenario in which the massive binary formed last, heating and evaporating the remaining gas, unbinding the cluster and terminating star formation – a scenario similar to the gas expulsion model for the unbinding and expansion of OB associations (e.g. Lada & Lada 2003; Goodwin & Bastian 2006). However, Eldridge (2009) updated the age of γ^2 Vel to 5.5 ± 1 Myr using models that take account of rotation and previous mass transfer between its binary components, weakening the evidence that it is younger than the surrounding low-mass stars.

The RVs obtained by J09 had comparatively low precision and could not resolve the association kinematics. The observed RV dispersion of 2.5 km s^{-1} was interpreted as mostly due to measurement uncertainties. Any intrinsic RV dispersion would be unable to explain the presence of stars over the full 10 degree diameter of Vela OB2 if they were intially in a much more compact configuration. Instead it was proposed that γ^2 Vel and its surrounding low-mass siblings are a subcluster within a larger star forming region responsible for Vela OB2.

In this paper we present initial results from GES for the Gamma Vel cluster, focused on the kinematics of its low-mass members. In Sect. 2 we describe the spectroscopic observations and the measurement of RVs. Included in this is an empirical estimate of the RV precision obtained by GES. In Sect. 3 we describe how we select a kinematically unbiased sample of cluster members and in Sect. 4 we present an analysis of the RV and spatial distribution of these members. In Sect. 5 we discuss our results in the context of the formation and evolution of the Gamma Vel cluster and its relationship with Vela OB2.

2. *Gaia*-ESO survey spectroscopy

2.1. Target selection and observations

The GES strategy for target selection within clusters is described in detail by Bragaglia et al. (in prep.). Low-mass targets in the direction of the Gamma Vel cluster were chosen primarily by their location in the $V - I/V$ and $B - V/V$ colour–magnitude diagrams (CMDs) using the 0.9 deg^2 photometric survey of J09. Targets with $12 < V < 19$ mag, corresponding to a mass range

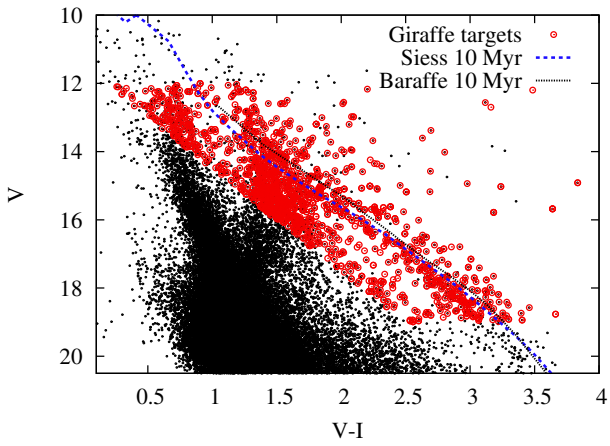

Fig. 1. Colour–magnitude diagram for unflagged objects with good photometry (uncertainties <0.1 mag in V and $V-I$) in a 0.9 deg^2 area around γ^2 Vel (from Jeffries et al. 2009). Objects with larger red symbols were observed in the GES. The lines shows theoretical 10 Myr PMS isochrones (from Siess et al. 2000; and Baraffe et al. 1998, using a colour–$T_{\rm eff}$ relation tuned to match the Pleiades) at an intrinsic distance modulus of 7.76, and with a reddening and extinction of $E(V-I) = 0.055$ and $A_V = 0.131$.

of $1.5 > M/M_\odot > 0.2$ (based on an intrinsic distance modulus of 7.76 ± 0.07, $E(B-V) = 0.038 \pm 0.016$, $A_V = 0.131$ from J09, an assumed age of 10 Myr and the evolutionary models of Siess et al. 2000), were selected from the region of the CMDs surrounding the known spectroscopic and X-ray selected members in J09. A very wide surrounding margin was considered to ensure that selection is not biased by these properties. The $V-I/V$ CMD of all stars is shown in Fig. 1, with the objects actually observed (see below) indicated.

The targets were observed with the FLAMES fibre-fed spectrographs at the VLT UT-2 (Kueyen) on the nights of 31 December 2011, 01-02 January 2012, and 14 February 2012. Both the UVES high-resolution and GIRAFFE intermediate-resolution spectrographs were used. More than 90 per cent of the spectra were obtained with GIRAFFE and we deal only with these data here. GIRAFFE was used in conjunction with the Medusa fibre system and the HR15n order-sorting filter, which gave spectra with a resolving power of 17 000 covering a common wavelength range of 6444–6816 Å.

Targets were grouped according to their V magnitude and configured for multi-fibre spectroscopy in 18 fields that covered the area of the photometric survey with significant overlap between fields. Depending on target brightness, these fields were observed in "observation blocks" (OBs) of 2×600 s or 2×1500 s. The two exposures were interleaved with a 60 s exposure in which 5 dedicated fibres were illuminated by a bright (compared with the stellar spectra) thorium-argon (ThAr) lamp. These short exposures, known as "simcal" observations, combined with much longer day-time ThAr lamp exposures that illuminated all the instrument fibres, formed the basis of a precise wavelength calibration. Approximately 20 fibres in each configuration were placed on blank sky regions and used during the analysis to subtract the sky contribution from each target spectrum. The times of observation, central positions, exposure times and number of targets for each OB are listed in Table 1.

A total of 1802 observations of 1242 unique targets were obtained. The overlap between fields meant that 353 targets were observed twice, 59 were observed 3 times, 23 were observed 4 times and 4 objects were observed on 6 occasions. These multiple observations were used to empirically judge the precision of the RV measurements. The survey covered 85 per cent of possible targets selected from the photometric survey; the majority of the unobserved targets have $12 < V < 16$ mag.

Table 1. A log of the VLT/Flames observations.

Date	UT	RA, Dec (field centre)	Exp time (s)	$N_{\rm targets}$
01 Jan. 2012	02:39:13	08:11:09.2–47:00:03	2×1500	106
01 Jan. 2012	03:45:07	08:09:10.5–47:02:24	2×1500	100
01 Jan. 2012	04:53:52	08:07:29.3–47:01:15	2×1500	65
01 Jan. 2012	05:59:32	08:11:21.2–47:01:49	2×600	113
02 Jan. 2012	02:22:15	08:10:59.8–47:20:19	2×1500	104
02 Jan. 2012	03:29:47	08:09:46.0–47:20:41	2×1500	111
02 Jan. 2012	04:33:33	08:07:45.9–47:21:07	2×1500	94
02 Jan. 2012	05:38:39	08:09:21.1–47:02:24	2×600	102
03 Jan. 2012	02:43:43	08:10:57.7–47:37:04	2×1500	95
03 Jan. 2012	03:49:09	08:09:22.4–47:37:03	2×1500	94
03 Jan. 2012	04:55:44	08:07:36.1–47:37:04	2×1500	66
03 Jan. 2012	06:00:44	08:07:41.6–47:02:58	2×600	108
15 Feb. 2012	01:20:04	08:11:11.8–47:25:05	2×600	113
15 Feb. 2012	01:55:33	08:09:43.8–47:21:38	2×600	113
15 Feb. 2012	02:30:39	08:07:47.8–47:18:50	2×600	114
15 Feb. 2012	03:08:03	08:10:59.4–47:37:03	2×600	111
15 Feb. 2012	03:43:01	08:09:20.1–47:35:46	2×600	112
15 Feb. 2012	04:18:28	08:07:20.6–47:41:06	2×600	81

2.2. Data reduction

Full details of the GES GIRAFFE data reduction will be given in a forthcoming paper (Lewis et al., in prep.). In brief, the raw data frames were corrected for a bias level using zero exposure bias frames and the images were divided by normalised daytime tungsten lamp exposures to remove pixel-to-pixel sensitivity variations. The multiple spectra on each frame were also traced using the tungsten lamp exposures and then extracted using the optimal algorithm described by Horne (1986). This algorithm also yields the estimated signal-to-noise ratio (S/N) in the extracted spectral pixels, given the readout noise and gain of the CCD, and it is this estimate that is propagated through subsequent analysis steps leading to the final reported S/N of the spectra. The extracted tungsten lamp spectra were used to correct the overall shape of the spectrum and calibrate the individual transmission efficiencies of each fibre.

The wavelength calibration proceeded in two stages. Deep exposures of a daytime ThAr arc lamp were used to define a polynomial relationship between extracted spectral pixel and wavelength, which typically returned an rms difference from the fit of 0.005 Å for about 20 lines used in each calibration. This relationship was subsequently modified by an offset determined from the positions of the most prominent arc lines in the short "simcal" exposures and by a barycentric correction. Spectra were rebinned into 0.05 Å pixels using this wavelength solution and sky was subtracted using a median of the sky spectra corrected for the differing responses of each fibre.

Several iterations of the data reduction were made including consistency checks between parallel but independent GIRAFFE reduction pipelines operated at the Cambridge Astronomical Survey Unit (CASU) and at Keele University. The analyses in this paper are based on the first internal data released by CASU to the GES consortium in July 2013 (GESviDR1Final) and placed in the GES archive at the Wide Field Astronomy Unit at Edinburgh University[1].

[1] http://ges.roe.ac.uk/

2.3. Radial velocities

RVs were determined using two techniques that will be fully described in a forthcoming paper (Koposov et al., in prep.). A first pass used a standard cross-correlation method with a grid of synthetic template spectra at a range of temperatures, metallicities and gravities (Munari et al. 2005) to give an initial RV estimate. The second pass used a direct modelling approach that fits each spectrum with a low-order polynomial multiplied by a template spectrum, with the RV, projected equatorial velocity ($v \sin i$), temperature, gravity, metallicity and polynomial coefficients as free parameters. An automated emission-line detection procedure excluded emission lines from the fitting process – predominantly the Hα line in young members of the Gamma Vel cluster. The best-fit was found by chi-squared minimisation, but the formal RV uncertainties estimated with this technique were found to be too small, chiefly due to systematic uncertainties in wavelength calibration.

2.3.1. Radial velocity precision

An accurate assessment of RV precision is key to the dynamical analysis of clusters. The format of the Gamma Vel observations lend themselves to a semi-empirical determination of the RV uncertainties. Repeated observations of a target in the same and different fibre configurations allow us to identify and assess various sources of error.

A series of simulations (see also Jackson & Jeffries 2010) suggest that the RV uncertainty, σ, has the following functional form

$$\sigma^2 = A^2 + B^2 \left[\frac{1 + (v \sin i / C)^2}{S/N} \right]^2, \quad (1)$$

where A, B and C are constants to be determined, $v \sin i$ is measured from the spectrum during the chi-squared fitting process (Koposov et al., in prep.) and S/N is the median signal-to-noise ratio per pixel of the spectrum derived during the extraction process. This formula allows for the expected decrease in precision with decreasing S/N and increasing $v \sin i$, but the A term also accounts for any systematic uncertainty associated with the wavelength calibration. We determine A, B and C in two stages.

(i) We consider 1770 pairs of exposures of the same object, taken within the same OB and where the combined spectrum has a $S/N > 5$. An estimate of the RV precision in the combined spectrum is given by $\sigma = |\Delta RV|/\sqrt{2}$, where ΔRV is the change in RV between the two exposures. We clip out 53 pairs with $|\Delta RV| > 2\,\mathrm{km\,s^{-1}}$. Figure 2 shows the rms value of σ as a function of S/N for the remaining pairs. A, B and C are estimated by fitting Eq. (1) to a surface of σ in the S/N vs $v \sin i$ plane. This yields $A = 0.09 \pm 0.01$, $B = 3.52 \pm 0.23$, $C = 38 \pm 8$ (all in units of $\mathrm{km\,s^{-1}}$). This means that within a single OB, the repeatability of RV measurements is $90\,\mathrm{m\,s^{-1}}$ for stars with high S/N and small $v \sin i$. Several loci determined using Eq. (1) with these coefficients are shown in Fig. 2 where the uncertainty is plotted versus S/N for binned data points with $v \sin i$ above and below $30\,\mathrm{km\,s^{-1}}$. Although the model is poorly constrained at high $v \sin i$ values where there is little data (95 per cent of the targets used have $v \sin i < 30\,\mathrm{km\,s^{-1}}$), it appears that rotational broadening has little effect below $30\,\mathrm{km\,s^{-1}}$, but uncertainties increase rapidly thereafter, with some indication that Eq. (1) underestimates the uncertainties for high $v \sin i$ and S/N by about 30 per cent.

(ii) The coefficients do not yet account for uncertainties in the wavelength calibration because an identical calibration is applied to each set of spectra within an OB. We assume that B and C are properties of the observed stars and the fitting process alone and can be applied to any spectrum. To estimate a value of A that takes account of wavelength calibration uncertainties we fix B and C and fit Eq. (1) to the RV differences from 329 pairs of observations[2] in *different* OBs, and where each contributing spectrum has a $S/N > 5$ and the OBs were taken within 3 days of each other. This latter condition minimises any variations caused by the motion of unresolved binary systems. Using a model binary distribution (see Sect. 4.1) we estimate that only one per cent of our targets are expected to be in unresolved binaries that have an RV that varies by between $0.5\,\mathrm{km\,s^{-1}}$ and $2\,\mathrm{km\,s^{-1}}$ (beyond which they are clipped in any case) on 3-day timescales. The bottom panel of Fig. 2 shows

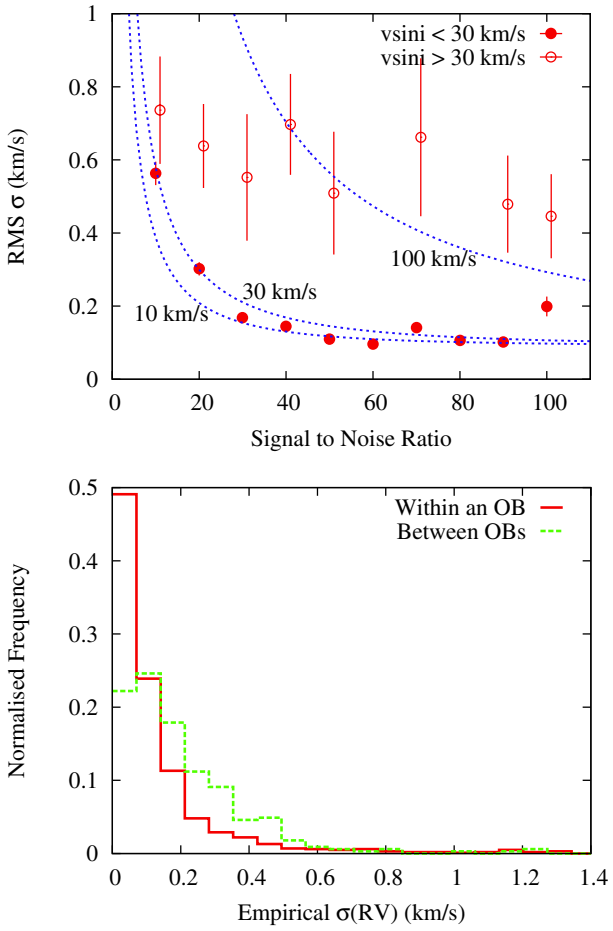

Fig. 2. Empirically determined RV precision. *Upper panel*: rms of the empirically estimated RV uncertainties (see text) from pairs of observations within an OB, binned by S/N. A separate set of points is calculated for stars that have an estimated $v \sin i > 30\,\mathrm{km\,s^{-1}}$ to demonstrate their larger empirical uncertainties. The lines on the plot are loci determined from Eq. (1) using the coefficients $A = 0.09 \pm 0.01$, $B = 3.52 \pm 0.23$, $C = 38 \pm 8$ for several labelled $v \sin i$ values. The fit is poorly constrained for large $v \sin i$ and there are some indications that the semi-empirical model underestimates the uncertainties for such stars at high S/N. *Lower panel*: frequency distribution of empirical RV uncertainties determined from repeated observations within an OB and from repeated observations from separate OBs. The increase in the width of the latter distribution indicates additional uncertainties associated with wavelength calibration between OBs.

[2] Where there are N (>2) observations of the same object we treat these as $N - 1$ independent pairs.

that the distribution of empirically estimated uncertainties becomes broader when considering repeat measurement from different OBs and we find $A = (0.246 \pm 0.029)$ km s^{-1}. The rms uncertainty increases from about 0.10 km s^{-1} for repeats within an OB to 0.28 km s^{-1} for repeats between OBs, though in both cases, a Gaussian distribution is not a good representation. There is a narrower core and longer tails, presumably because of stars with low S/N and/or high $v \sin i$. This is accounted for by our model and is why in our subsequent modelling we assign an individual RV uncertainty to each star, based on Eq. (1), rather than using a single average value.

The B and C coefficients derived here will be specific to the wavelength range and types of star observed. However, we anticipate that in most cases the GES RV precision will be dominated by the A coefficient and so the estimates provided here are likely to be widely applicable to late-type stars observed in GES with the same instrumental configuration. Early-type stars with fewer spectral features and often rapid rotation will have less precise RVs that are determined by their own particular B and C coefficients.

2.4. Lithium equivalent widths

The GESviDR1Final spectra include the Li I 6708Å feature that can be used as a membership indicator (see Sect. 3). The GES analysis (described in more detail in a forthcoming paper; Lanzafame et al., in prep.) uses three independent methods for deriving the equivalent width of this feature in the GIRAFFE spectra (hereafter referred to as EW(Li)): direct profile integration as implemented in SPLOT as part of the IRAF package[3], DAOSPEC (Stetson & Pancino 2008) and an ad hoc procedure written in IDL (E. Franciosini, priv. comm.). The latter automatically derives EW(Li) and its uncertainty by a direct profile integration taking into account the star's RV, $v \sin i$, and S/N. The analyses were performed on the summed spectra of each object.

The results obtained by the three different methods were first compared to check for systematic differences before combining them to produce the final results. Above 300 mÅ the DAOSPEC results were discarded because they systematically underestimated EW(Li) in FGK stars and overestimated it in M stars and fast rotators with respect to the results obtained using IRAF (probably because the strong line is non-Gaussian – see Pancino & Stetson 2008). In this range the final EW(Li) is given as the average between the IRAF value and IDL procedure. Below 300 mÅ the results obtained by the three methods were averaged, eventually discarding one of the three values if it deviated by more than one standard deviation. The uncertainty on the final EW(Li) is given conservatively as the larger of the standard deviation or the average uncertainty from the independent measurements. The median uncertainty of a detected Li line is 14 mÅ with a median S/N of 36. Where no significant EW(Li) can be found, an upper limit is estimated using the approach suggested by Cayrel (1988). As each of the three EW estimation procedures uses an independent approach to establishing a continuum level, the quoted uncertainties automatically contain some allowance for uncertain continuum placement and this is the dominant source of uncertainty even at the median S/N.

The standard GES analysis of EW(Li) also makes an attempt to account, where necessary, for blending with a nearby weak Fe I line (Soderblom et al. 1993) and, in only 14 cases, the presence of a veiling continuum that is presumably due to accretion and diminishes the measured EW(Li). We ignore both of these corrections in the present analysis, using only the "raw", blended EW(Li) that is reported in the GESviDR1Final tables, but have confirmed that their inclusion would have made no difference to the selection of members described below.

[3] IRAF is written and supported by the National Optical Astronomy Observatories (NOAO) in Tucson, Arizona. NOAO is operated by the Association of Universities for Research in Astronomy (AURA), Inc. under cooperative agreement with the National Science Foundation.

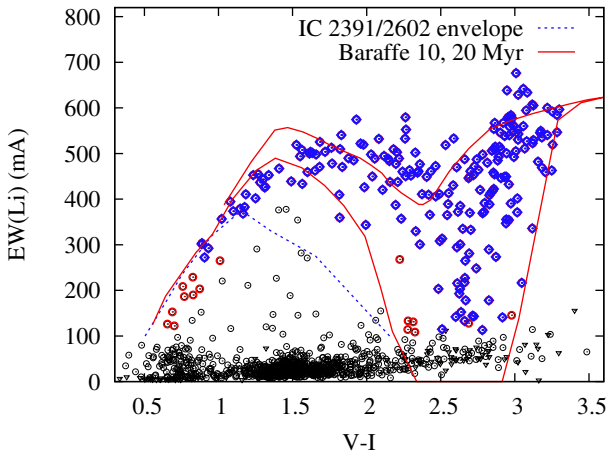

Fig. 3. Equivalent width of the Li I 6708 Å feature (EW(Li)) versus $V - I$. Objects selected as candidate members are marked with blue diamonds; red circles mark objects that are potential members based on their photospheric Li content, but fall outside the sequence of members in the colour–magnitude diagram (see Fig. 4). Triangles mark upper limits. The solid red lines show theoretical isochrones at 10 Myr and 20 Myr from the models of Baraffe et al. (1998, see text), reddened with $E(V - I) = 0.055$. The dashed line marks the upper envelope of EW(Li) for IC 2391 and IC 2602 at ages ≃50 Myr.

3. Membership selection

For this paper, our aim is to select a sample of association members as free from any kinematic bias as possible. The initial selection of candidate members therefore *did not* use the RV results. Instead we rely on the presence and strength of the Li I 6708 Å feature and the position of candidates in the $V - I/V$ CMD.

Lithium is a well-known age indicator for young PMS stars because it is rapidly depleted if the temperature at the base of the convection zone, or core of a fully convective star, exceeds $\simeq 3 \times 10^6$ K (e.g. Soderblom 2010). Theoretical isochrones of Li depletion have been calculated (e.g. Baraffe et al. 1998; Siess et al. 2000), but are subject to significant uncertainties regarding convective efficiency and atmospheric opacities. The models match the broad picture that has emerged from observations of Li abundances in young clusters, but do not agree with each other and cannot explain the significant scatter in Li abundance often seen in stars with similar age and $T_{\rm eff}$. Here we adopt an empirical approach and use a large EW(Li) as the principal criterion for selecting cluster members. The timescale for significant Li depletion ranges from ∼10–20 Myr in mid-M stars, ∼100 Myr in K-type stars, to ∼1 Gyr in G-type stars. Thus, the presence of Li will exclude the vast majority of field K- and M-dwarfs, but will not be as effective at excluding contaminating field G dwarfs.

Figure 3 shows EW(Li) plotted against $V - I$ colour compared with 10 and 20 Myr isochrones calculated from the evolutionary models of Baraffe et al. (1998 – with mixing length

Table 2. Coordinates, photometry and measurements of RV, EW(Li), $v \sin i$ and estimated masses for 208 targets selected as Gamma Vel members.

CNAME	RA	Dec (J2000)	V	$V-I$	S/N	N	EW(Li)	ΔEW(Li) (mÅ)	RV	σRV (km s^{-1})	P_A	$v \sin i$ (km s^{-1})	$M/M_\odot$
08064077-4736441	08:06:41	−47:36:44	13.48	1.31	135	1	425.8	1.7	61.14	0.25	−1.0	1.2	1.23
08064390-4731532	08:06:44	−47:31:53	17.65	2.67	21	1	178.2	14.3	16.54	0.31	0.85	13.7	0.45
08065007-4732221	08:06:50	−47:32:22	18.22	2.72	13	1	452.7	22.0	20.89	0.37	0.05	1.0	0.43

Notes. The full table is available in electronic format at the CDS; a sample is shown here. N is the number of individual observations contributing to the mean values quoted. P_A is the probability that the star belongs to kinematic population A, but is set to −1 if the RV is outside the range 8 to 26 km s^{-1}. Although values of $v \sin i < 10$ km s^{-1} are reported in the GESviDR1Final tables, we suspect that subsequent analysis will likely suggest these are unreliable and we treat them as upper limits at 10 km s^{-1} in Sect. 4.2.4. Masses are estimated from the $V-I$ colour and models of Baraffe et al. (1998) for an assumed age of 10 Myr.

of 1.0 pressure scale heights). The model Li abundances are folded through the NLTE curves of growth described in Jeffries et al. (2003), based on ATLAS9 models for warmer stars ($T_{\rm eff} >$ 4000 K, Kurucz 1993) and from Zapatero-Osorio et al. (2002) for $T_{\rm eff} \leq 4000$ K. The relationship between $T_{\rm eff}$ and $V-I$ is also that used in Jeffries et al. (2003 – see their Fig. 6) and we redden the models by $E(V-I) = 0.055$. The 20 Myr isochrone is a *guide* to the lowest EW(Li) we might expect from Gamma Vel cluster members, but must be used with caution given the sensitivity of such models to convective efficiency and the details of the atmosphere and curves of growth. A further empirical locus marks the observed upper envelope of EW(Li) in the clusters IC 2391 and IC 2602 (Randich et al. 1997, 2001), that have ages of about 50 Myr and which we expect more definitely define a lower boundary for association members. $E(V-I)$ values of 0.01 and 0.04 were assumed for these clusters (Patten & Simon 1996). Caution is still warranted in stars with $V-I < 1.5$, where any small systematic differences in the EW(Li) measurements between our work and the literature samples (e.g due to the continuum definition, or how rapid rotation is dealt with) could be comparable to the Li depletion expected between 10 and 50 Myr.

The larger symbols (both blue diamonds and red circles) in Fig. 3 show those objects we initially select as Gamma Vel cluster members on the basis of EW(Li) and the loci discussed above. A significant detection of the Li line with EW(Li) > 100 mÅ was taken as an absolute criterion. Contamination by Li-rich field giants is still possible, but is ignored because only ∼1 per cent of G/K giants might exhibit photospheric Li at a level that meets our threshold (Brown et al. 1989). The Li-selected targets are then passed through a further filter in the $V-I/V$ CMD (shown in Fig. 4). Here, the purpose is to exclude Li-rich objects that appear to lie well away from the locus defined by most cluster members. Figure 4 shows that, as expected, the presence of Li in G stars is not a reliable indication of cluster membership and most of these have been excluded by the CMD filtering. Few stars at cooler spectral types are excluded in the CMD because field stars at these temperatures are rarely expected to retain Li at the levels we demanded in Fig. 3.

The definition of these two filters is to some extent arbitrary, our concern is mainly to avoid contamination by field stars. We note that it is possible that we have excluded a few genuine cluster members. These might be objects that are displaced in the CMD by variability or their photometric uncertainties, but our filter should not exclude unresolved binaries. It is also possible we have excluded a few objects that have an apparently weak Li line due to very rapid rotation or, particularly around $V-I \sim 2.7$, have actually depleted Li beyond the limits we have accepted. On the basis of the RVs of excluded objects and the small fraction of objects showing evidence for rapid rotation in our sample, the numbers of excluded genuine members is unlikely to amount to more than a few per cent of the accepted sample.

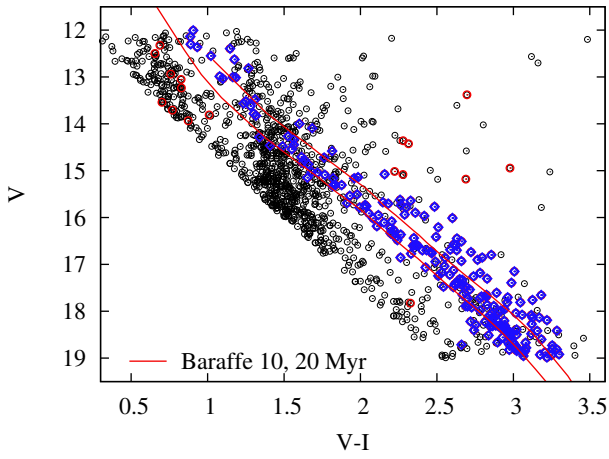

Fig. 4. Colour–magnitude diagram for the Gamma Vel targets. Blue diamonds show the Li-rich targets we select as members (see Fig. 3); red circles are Li-rich targets that do not follow the sequence defined by the bulk of cluster members and are excluded. Solid red lines show isochrones from the Baraffe et al. (1998) evolutionary models (see text), shifted to a distance modulus of 7.76 mag, with reddening $E(V-I) = 0.055$ and extinction $A_V = 0.131$ applied.

4. Results and analysis

All the data for all the targets observed in the Gamma Vel OBs listed in Table 1, including the EW(Li) values, photometry (from J09) and RVs (including RVs determined from individual exposures and from OBs) can be obtained from the *Gaia*-ESO archive hosted by the Edinburgh University Wide Field Astronomy Unit. Results for the 208 Gamma Vel members selected in Sect. 3 are reported in Table 2 (available in electronic format). For each cluster member we report the weighted mean RV (weighted by the uncertainties calculated from Eq. (1) for each contributing OB) and its total calculated uncertainty, the mean rotational broadening and the total S/N (across multiple OBs where appropriate) and the mean EW(Li) and its uncertainty obtained as described in Sect. 2.4. Figure 5 shows the distribution of calculated RV uncertainties for the Gamma Vel members. The median uncertainty is 0.26 km s^{-1}. The obvious bimodality arises from the 80 objects with more than one independent observation and consequently smaller final RV uncertainties.

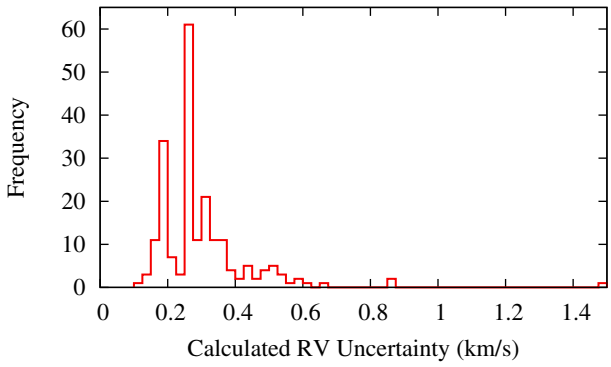

Fig. 5. Distribution of RV uncertainties for the selected Gamma Vel members, calculated using Eq. (1). Where objects were observed in more than one OB, the uncertainty in the weighted mean RV is correspondingly smaller.

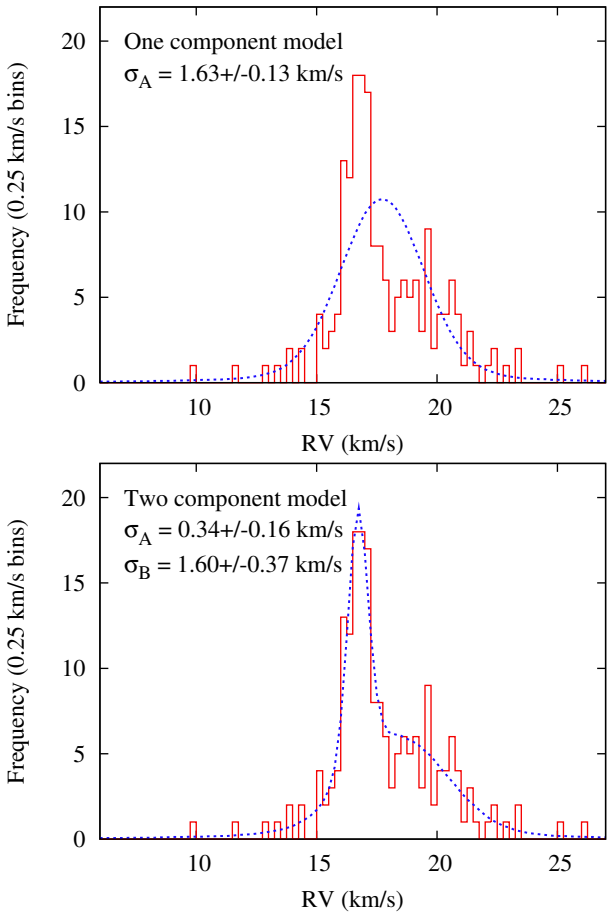

Fig. 6. Binned RV histogram for the Gamma Vel members (note that fitting was carried out on unbinned data). *Upper panel*: the best fit for a model consisting of a single Gaussian population with a fraction $f_{\rm bin} = 0.46$ of unresolved binaries (see text). The fit is poor. *Lower panel*: the best fit for a population represented by two Gaussian components, each with an unresolved binary population.

4.1. Modelling the radial velocity distribution

A histogram of the mean RVs for stars selected as members is shown in Fig. 6 and is modelled using a maximum likelihood technique. We implicitly assume that our membership selection procedure has excluded unassociated field stars. A complication is that some fraction of these objects will be unresolved binary systems. The procedure we adopt is described in detail by Cottaar et al. (2012b) but is summarised here with some minor differences highlighted.

We assume that the observed RVs are drawn from an intrinsic distribution that is broadened by measurement uncertanties and the possibility of binary motion. Single stars and the centres of mass for binaries are assumed to share the same intrinsic RV distribution. The likelihood of a star's observed RV, v_i, given an intrinsic RV distribution and the estimated RV uncertainty, σ_i is

$$L_i(v_i) = (1 - f_{\rm bin})\, L_{\rm single}(v_i, \sigma_i) + f_{\rm bin}\, L_{\rm binary}(v_i, \sigma_i), \quad (2)$$

where $f_{\rm bin}$ is the fraction of observed objects that are unresolved binaries; $L_{\rm single}$ is the convolution of a model intrinsic RV distribution with a Gaussian of dispersion σ_i; and $L_{\rm binary}$ is the equivalent likelihood distribution for binary systems, but is calculated after convolving the model intrinsic RV distribution with an uncertainty *and* the distribution of velocity offsets expected from a set of randomly oriented SB1 binary systems, with a specified distribution of orbital periods and eccentricities.

For binaries, we assume $f_{\rm bin} = 0.46$, a lognormal period distribution, a mean $\log P = 5.03$ (in days) and dispersion 2.28 dex, with a flat mass ratio distribution for $0.1 < q < 1$ (Raghavan et al. 2010). For ease of computation we consider only circular orbits; tests using an eccentricity distribution showed that it has no significant effect on the results. The binaries are assumed to have a random orientation in space and to be observed at a random phase of their orbits. Monte Carlo simulations give a distribution of observed RV offsets for the primary star with respect to the binary centre of mass. The calculation was performed separately for each target, assuming a primary mass (given in Table 2) approximated by interpolating its $V - I$ colour along a 10 Myr Baraffe et al. (1998) isochrone and a system mass a factor of $(1 + q)$ larger[4].

Given a model intrinsic RV distribution described by a number of free parameters (see below), the best-fitting model is found by calculating the likelihood for each star (from Eq. (2)) and then maximising the summed log likelihood for all stars by varying the parameters over a grid of possible values. Uncertainties in a parameter are calculated from the distribution of maximum log likelihoods for that parameter evaluated after optimisation with respect to all other model parameters.

4.1.1. A single Gaussian population

We begin by considering an intrinsic RV distribution modelled with a single Gaussian of width $\sigma_{\rm A}$ and centre $RV_{\rm A}$. The fit was made only to data with weighted mean RV between 8 and 26 km s^{-1}. There are 18 objects that lie outside this range. All must be considered candidate binary systems. Only four have multiple measurements, but these do not show evidence of RV variability at the 1 km s^{-1} level. The most likely fit to the remaining 190 objects has $\sigma_{\rm A} = 1.63 \pm 0.13$ km s^{-1} and $RV_{\rm A} = 17.71 \pm 0.14$ km s^{-1}. An approximation[5] to this model is shown in Fig. 6, where the intrinsic distribution has been broadened by the mean uncertainty profile (note that this is not the same as a Gaussian with a dispersion equal to the mean RV uncertainty)

[4] We initially performed the analysis using a fixed mass of 1 $M_\odot$. The best-fitting intrinsic RV distributions and parameters differed by much less than the uncertainties in the best-fitting parameters presented here, indicating that the procedure is quite robust to mass uncertainties.

[5] In the maximum likelihood fitting, each star has its own RV uncertainty, but we have to assume some mean level of uncertainty to broaden the intrinsic RV distribution for plotting purposes.

Table 3. Results of the maximum likelihood RV modelling.

	One component	Two components
RV_A (km s^{-1})	17.71 ± 0.14 (17.72)	16.73 ± 0.09 (16.72)
σ_A (km s^{-1})	1.63 ± 0.13 (1.62)	0.34 ± 0.16 (0.30)
σ_B (km s^{-1})		1.60 ± 0.37 (1.85)
ΔRV_{AB} (km s^{-1})		2.15 ± 0.48 (1.88)
f_A		0.48 ± 0.11 (0.43)
ln L_{max}	−416	−395
P_{KS}	0.006	0.994

Notes. Symmetric 68 per cent confidence intervals for one parameter of interest, the value at the maximum likelihood fit is given in brackets. RV_A is the centre of the first (or only) velocity component; σ_A and σ_B are the *intrinsic* velocity dispersions of the first and second component; ΔRV_{AB} is the velocity separation of the two components; f_A is the fraction of stars belonging to the first component; ln L_{max} is the log likelihood value for the best fit and P_{KS} is the probability that the data are drawn from the model as judged by a Kolmogorov-Smirnov test (see text).

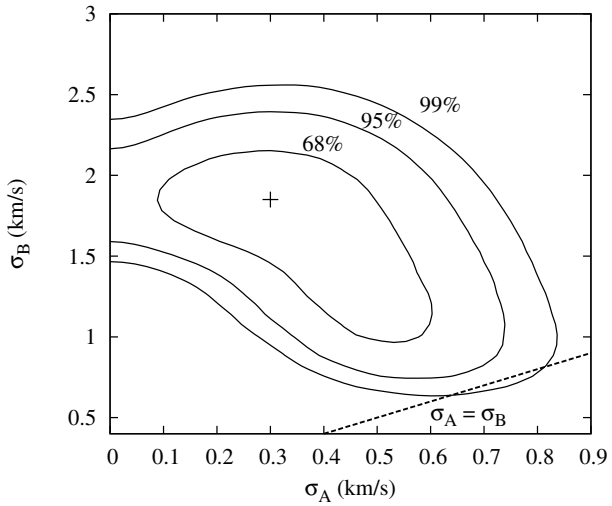

Fig. 7. Likelihood space for σ_A versus σ_B for the two-Gaussian fit to the RV distribution. Confidence contours are shown for two parameters of interest. $\sigma_B > \sigma_A$ with a high degree of confidence.

and a fraction (f_{bin} = 0.46) of the model realisations are broadened due to binary motion as described earlier. The fit looks poor, but maximum likelihood fitting does not yield a "goodness of fit" parameter. Instead we have compared the cumulative RV distributions of data and model using a Kolmogorov-Smirnov (KS) test, which rejects the hypothesis that the data are drawn from the model distribution with 99.4 per cent confidence.

4.1.2. A two-component model

The data suggest the addition of a second Gaussian component. We refer to the two components, or populations, as A and B. With the binary parameters fixed, this model has 5 free parameters: the central RV of one population, RV_A, the difference in central RV of the two components ΔRV_{AB}, the Gaussian dispersions of the two components σ_A and σ_B and the fraction of stars that belong to the first component f_A. It is assumed that the stars belong to one component or the other so that $f_B = 1 - f_A$. The likelihood of observing a given RV is now

$$L_i = f_A\, L_{A,i} + (1 - f_A)\, L_{B,i}, \quad (3)$$

where L_A and L_B are likelihoods calculated using Eq. (2), but with the appropriate intrinsic model RV distributions for components A and B respectively.

The values of the parameters at the maximum likelihood fit are given in Table 3 along with symmetric 68 per cent confidence intervals for a single parameter of interest. An approximation to the best-fitting model (calculated using the mean uncertainty profile) is shown in the lower panel of Fig. 6 and consists of roughly equal numbers of stars in each component, one with a very narrow intrinsic dispersion and the other much broader and offset by 2.15 km s^{-1}. The maximum log likelihood increases by 21 with this more complex model at the cost of three additional degrees of freedom. Using the Wilk's theorem approximation, the two component model is preferred over the single component model with 99.99 per cent confidence. The two component model is also preferred according to the Bayesian information criterion. A KS test yields P_{KS} = 0.994, suggesting the data and model are consistent and that searching for more complex structure is unlikely to yield further significant improvement.

Whilst there are roughly equal numbers of stars belonging to each of the two components (f_A = 0.48 ± 0.11), their RV dispersions are quite different. To test whether correlations between the various parameters might affect this conclusion Fig. 7 shows the maximum likelihood space in the σ_A versus σ_B plane. Confidence contours are calculated according to the usual increments in log likelihood for *two* parameters of interest. We find there is no strong correlation and that $\sigma_B > \sigma_A$ with a high degree of confidence. Similarly, we find that the two components have different RV centroids with a high degree of confidence; i.e. $\Delta RV_{AB} > 0$.

The binary parameters we have used in our models come from a study of solar-type field stars. About half our sample has lower masses and there is some evidence that the binary frequency is smaller for such objects – perhaps 30 per cent (Duchêne & Kraus 2013). In any case, there may also be some difference in binary parameters associated with birth environment, so it is prudent to investigate the sensitivity of our results to this. We repeated the analysis with a binary frequency of 30 per cent. The main difference is that σ_B increases from 1.60 km s^{-1} to 1.89 km s^{-1}, a change that is less than the original uncertainty estimate. All other parameters change by much less than the uncertainties listed in Table 3, so we conclude that the results are quite insensitive to plausible uncertainties in the binary parameters.

4.2. Two populations in the Gamma Vel cluster?

Having established (at least) two kinematic components in the RV distribution of Gamma Vel members, we can ask whether there are any other properties that might distinguish these populations. We consider the CMD, the spatial distribution, the lithium depletion, rotational broadening and proper motions. In each case it is necessary to distinguish between members of the two populations, but this can only be done in a probabilistic way. For our two-component model we can calculate, for each star, the probability that it belongs to either populations A or B as

$$P_{A,i} = f_A \frac{L_{A,i}}{L_i} \qquad P_{B,i} = (1 - f_A)\frac{L_{B,i}}{L_i}, \quad (4)$$

where the terms are as defined in Eq. (3). This could be calculated for the maximum likelihood model, but we obtain a more

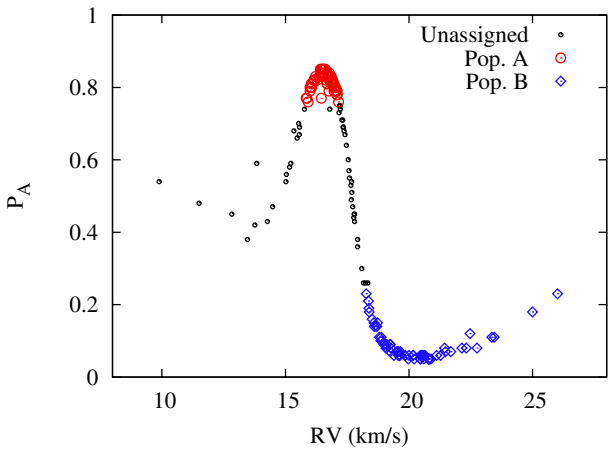

Fig. 8. Probability that each Gamma Vel member belongs to population A in the two-component kinematic model described in Sect. 4.1.2. Relatively secure members of population A ($P_A > 0.75$) and B ($P_A < 0.25$) and objects that cannot be confidently assigned to either population are identified with different symbols in this and subsequent plots.

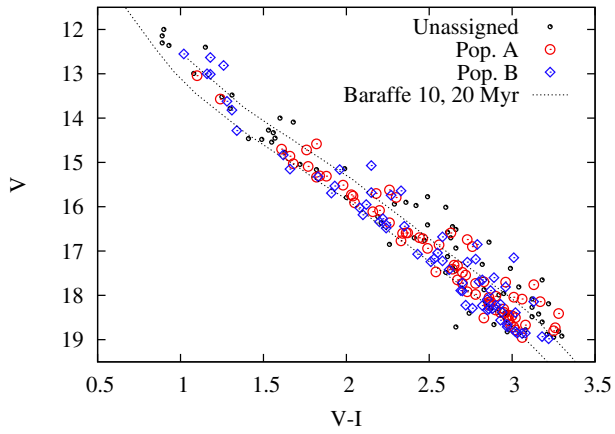

Fig. 9. Colour–magnitude diagram for the two kinematic populations around γ^2 Vel. The populations are distinguished here by a simple probability criterion (see Sect. 4.2) into population A (with a narrow RV distribution) or population B (with a broader RV distribution). The other cluster members cannot be assigned to either population with great confidence.

accurate estimate by integrating this probability over the full 5D parameter space and then $P_{A,i}$ is found from the expectation value of the total probability distribution function. $P_{B,i}$ is given by $1 - P_{A,i}$. The results of this calculation are illustrated in Fig. 8 and listed in Table 2 for each star. Stars outside the range $8 < RV < 26$ km s^{-1} are not considered and given $P_A = -1$. P_A depends mainly on the RV of the star but also to a lesser extent on the RV uncertainty. To test for differences in properties between the two populations we adopt two approaches. (i) Where appropriate, we use P_A and P_B as statistical weights in determining mean properties; (ii) for plotting purposes and also as a way of more carefully cleaning the samples of contamination, we divide the sample into a population of 73 objects having $P_A > 0.75$, which we will call population A, though we understand it will still have ≃19 per cent contamination by stars in the other population, and 66 stars with $P_A < 0.25$ that we call population B, but will have ≃9 per cent contamination from the other population (see Fig. 8). The remaining 69 objects cannot be assigned to either population with great confidence and are plotted with different symbols.

4.2.1. The colour–magnitude diagram

Figure 9 shows the $V - I/V$ CMD for members, coded for populations A or B according to the probabilistic criterion described above. The unassigned objects and objects with RV outside the range $8 < RV < 26$ km s^{-1} are also shown for completeness. We fit the distribution of points with a quadratic in $V - I$ for $V - I > 1.5$ mag, as the few points bluer than this define a kink in the diagram that is poorly reproduced by a polynomial. Fixing the linear and quadratic terms, we then fit populations A and B separately, allowing a constant offset. If the division is carried out as in Fig. 9, the difference in offsets for the two populations is a marginal 0.06 ± 0.07 mag in the sense that population A is brighter. If instead we perform fits weighted according to the probability of membership of populations A or B, this difference becomes 0.02 ± 0.03 mag. At an age of about 10 Myr the latter result and the Baraffe et al. (1998) isochrones plotted in Fig. 9 imply that population A is younger than population B by about 0.4 ± 0.6 Myr if they are at the same distance and have the same unresolved binary frequency. Alternatively, if they both have the same age, then population A is closer by 4 ± 5 pc.

A KS test of the mass distributions of the two populations resolved according to the probability criteria, reveals no significant difference ($P_{KS} = 0.84$). There are 8 higher mass objects in population B with $V - I < 1.5$, and only 2 in population A. This difference is not regarded as significant by a KS test though it is marginally significant (at the 95 per cent level) using a two-tailed Fisher test.

4.2.2. The spatial distribution

Figure 10 examines the projected spatial distributions of the two populations, with different symbols corresponding to the populations as in Fig. 9. The position of γ^2 Vel is marked. The most obvious difference between the populations is their centroid. Population A has a centroid of (RA = 122.413 ± 0.034, Dec = −47.378 ± 0.027), whilst the centroid of population B is at (RA = 122.305 ± 0.038, Dec = −47.381 ± 0.032). The distributions of the two populations are different in RA according to a KS test ($P_{KS} = 0.03$), but not in Dec ($P_{KS} = 0.64$). Accompanying this shift there appears to be an increase in RV of ∼2 km s^{-1} for population B towards the south-west. A weighted linear fit of RV versus position for the population B objects gives a slope of -0.28 ± 0.60 km s^{-1} deg^{-1} in the RA direction and -1.80 ± 0.68 km s^{-1} deg^{-1} in the Dec direction. No drifts are apparent for population A. The best fitting lines are shown in Fig. 10.

There is a hint that population A is more centrally concentrated than population B. The centroid of population A is consistent with the position of γ^2 Vel, whilst the centroid of population B is separated from γ^2 Vel by 4.1±2.3 arc minutes. A KS test of the distributions of radial distance from γ^2 Vel reveals only a marginal difference with $P_{KS} = 0.15$. A central concentration in either population might be due to biases in the target selection. To check this we examined the spatial distribution of targeted objects *not* considered to be Gamma Vel members in Sect. 3, because these should be subject to a similar spatial bias in target selection, but should have an approximately uniform intrinsic spatial distribution. The normalised distributions of spatial density with radius for populations A, B and the targeted non-members are shown in Fig. 11. Population A is more centrally concentrated than the target population, with a significantly different

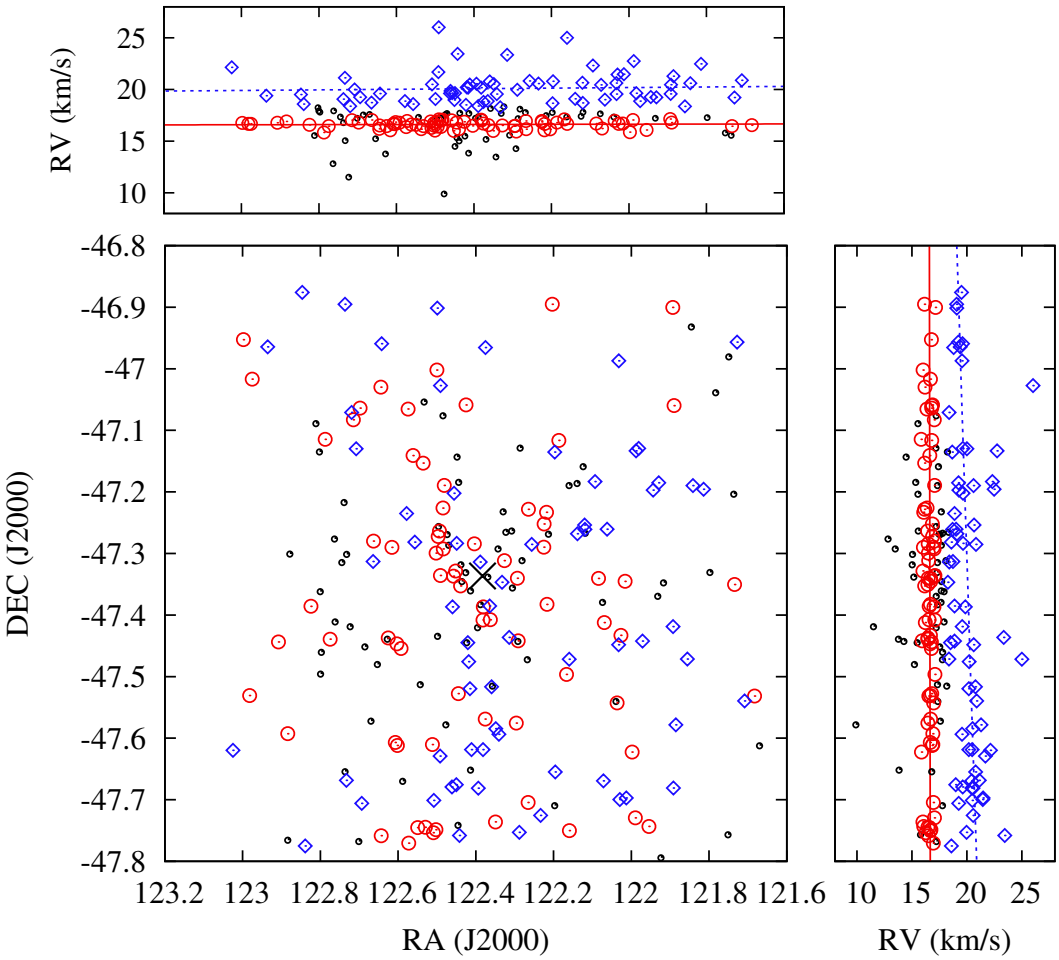

Fig. 10. Spatial distribution of populations A and B, defined according to the probability criterion described in Sect. 4.2. In the *main panel* these populations and the set of cluster members that cannot be confidently assigned to either are shown. Symbols are as defined in Fig. 9. The cross marks the position of γ^2 Vel. In the *top* and *side panels* we show the distribution of RV with right ascension and declination respectively. The solid (red) lines and the dashed (blue) lines show best-fitting linear relationships for populations A and B respectively.

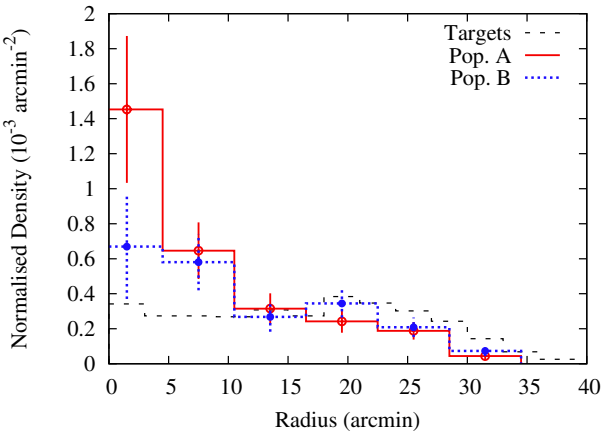

Fig. 11. Projected space density of members of populations A and B, along with that of all the (non-members of the Gamma Vel cluster) targets observed. Population A is more centrally concentrated than population B, though the significance of this is low (see Sect. 4.2.2).

radial distribution ($P_{KS} < 10^{-5}$). Population B is also more centrally concentrated than the targets, but less so than population A ($P_{KS} = 0.02$). Given that it is still contaminated with ≃6 stars from population A, it is conceivable that population B has a quite similar spatial distribution to the general field population and that population A, which has ∼13 contaminants from population B, is even more centrally concentrated. If we use P_A and P_B to weight the contributions from all stars, we find the mean radial distances from γ^2 Vel are 15.2 ± 0.6, 18.8 ± 1.0 and 21.8 ± 0.2 arcminutes for populations A, B and the targeted non-members respectively.

In summary then, Population A has a centroid consistent with the position of γ^2 Vel, is definitely more centrally concentrated than the observed targets and probably more centrally concentrated than population B. The centroid of Population B is offset from population A by 4.4 ± 3.0 arcminutes and has a spatial distribution that is marginally consistent with either population A or the observed targets. Population B shows significant evidence for a spatial gradient in RV in the declination direction.

4.2.3. Lithium depletion

Figure 12 shows the EW(Li) versus colour plot, with the Gamma Vel members separated by population as described in Sect. 4.2. There is a suggestion in this plot that population A is more Li-depleted than population B, especially in the range $2.5 < V - I < 2.8$ where age-dependent Li-depletion is expected to be strongest.

The statistics bear this conclusion out. The weighted mean EW(Li) for stars with $2.5 < V - I < 2.8$ is 269 ± 21 mÅ for

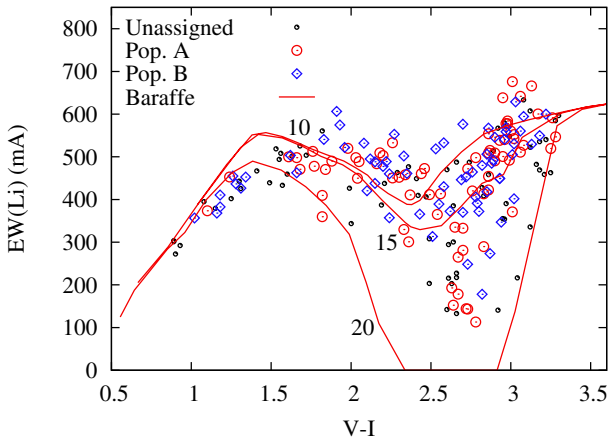

Fig. 12. Equivalent width of the Li I 6708 Å line versus colour, with different symbols corresponding to the populations as in Fig. 9. The solid lines are isochrones calculated according to the evolutionary models of Baraffe et al. (1998, with mixing length of 1.0 pressure scale heights) at 10, 15 and 20 Myr, transformed into the observational plane as described in Sect. 3.

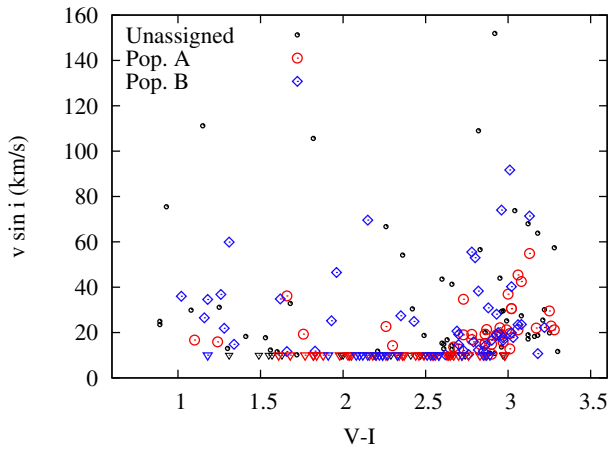

Fig. 13. Projected rotational velocities as a function of colour. The different symbols correspond to the various populations as described in Fig. 9. Objects with $v \sin i < 10\,\mathrm{km\,s^{-1}}$ are marked as upper limits (triangles).

population A and 433 ± 19 mÅ for population B. If we use the whole sample, but apply a further weighting according to the probability of membership of populations A or B, the results for the mean EW(Li) in this colour range are 303 ± 17 mÅ for population A and 413 ± 15 mÅ, a smaller difference, but still significant at the 5-sigma level. Hence this result is quite robust to the details of how membership of the two populations is assigned.

The difference in Li-depletion implies a difference in age. Population A would need to be older (on average) by an amount which is dependent on the the way that EW(Li) is translated into a Li abundance. Because the Li I 6708 Å line is in the saturated part of the curve of growth, a small change in EW(Li) corresponds to a large change in Li abundance (Palla et al. 2007), but Li-depletion is also very rapid at these masses, so a large change in abundance is expected in a small amount of time. Adopting the models of Baraffe et al. (1998) and the isochrones shown in Fig. 12, which at least match the colour of dip in Li abundance quite well, we see that rapid depletion commences at ∼10 Myr and the small EW(Li) difference we have found could correspond to only ∼1–2 Myr in mean age. The absolute age at which rapid Li depletion commences is model dependent and begins earlier (but at bluer colours) for models with higher convective efficiencies, but the implied age difference of ∼1–2 Myr is reasonably robust to choice of model. That there are examples of Li-depleted and undepleted stars in both populations with $2.5 < V - I < 3$ might suggest that age spreads are larger than any age difference. Alternatively it might simply reflect that the samples identified in Fig. 12 are still cross-contaminated by the other population.

Another possibility is that the differences in photospheric Li are due to composition rather than age differences. Li depletion is predicted to be very sensitive to interior opacity and if Population A were even only 0.1 dex more metal-rich than Population B this might explain the observed difference (e.g. Piau & Turck-Chièze 2002). A detailed compositional analysis of the Gamma Vel cluster GES UVES data is underway (Spina et al., in prep.). A detailed discussion of the Li abundances and comparison with models is deferred to Franciosini et al. (in prep.); the important point here is that there *is* a difference between populations A and B.

4.2.4. Rotation rates

Figure 13 shows the projected equatorial velocities of the sample as a function of colour. Values of $v \sin i < 10\,\mathrm{km\,s^{-1}}$ are unlikely to be accurate, given the resolution of the spectra, and are regarded as limits of $<10\,\mathrm{km\,s^{-1}}$. There is a hint that members of population B are more rapidly rotating, on average, especially for $V - I < 2.5$ mag, but the numbers are small. A two-tailed KS test of the cumulative $v \sin i$ distributions reveals a marginal difference ($P_{\mathrm{KS}} = 0.12$). Even if the two populations had different ages, it is unlikely that this comparison would be diagnostic, because the timescale of rotation spindown with age is too slow (∼50 Myr) at the masses of the sample we consider. Any differences are more likely to reflect different birth conditions.

4.2.5. Proper motions

The catalogue of Gamma Vel members was matched with the Fourth US Naval Observatory CCD Astrograph Catalog (UCAC4, Zacharias et al. 2013). There were 92 matches within 1 arcsecond, most members brighter than $V \sim 17$ had a match. Figure 14 shows the vector point diagram with population A and B indicated. There are a number of very discrepant points. We have examined these stars individually and there are reasons to be suspicious about all of them; either they appear as blended, unresolved binaries on photographic plates or they are very close to γ^2 Vel itself. Clipping the sample between $-20 < PM(\mathrm{RA}) < 5$ mas/yr and $-10 < PM(\mathrm{Dec}) < 25$ mas/yr we obtain mean proper motions of (−5.9 ± 0.8, +8.6 ± 1.0) and (−4.5 ± 1.0, +8.7 ± 0.9) mas/yr for populations A and B respectively. The standard deviations for populations A and B are both ≃4.5 mas/yr in each coordinate, corresponding to ≃7 km s^{-1} at the distance of γ^2 Vel. This is only slightly larger than the respective mean proper motion uncertainties and incapable of resolving differences in tangential velocity dispersion comparable to that seen in the RV dispersions. If the proper motions are weighted by the probability of population membership, the mean proper motions of populations A and B are (−5.9 ± 0.8, +8.5 ± 1.0) and (−4.6 ± 1.0, +8.7 ± 0.9) mas/yr respectively.

These mean proper motions are similar to each other and also similar to the proper motion of γ^2 Vel (−5.9 ± 0.4, +9.9 ± 0.4 mas/yr; from HIPPARCOS) and the mean proper motion of early type stars in Vela OB2 (−6.6 ± 1.3, +8.1 ± 1.4 mas/yr; Tycho proper motions compiled by J09).

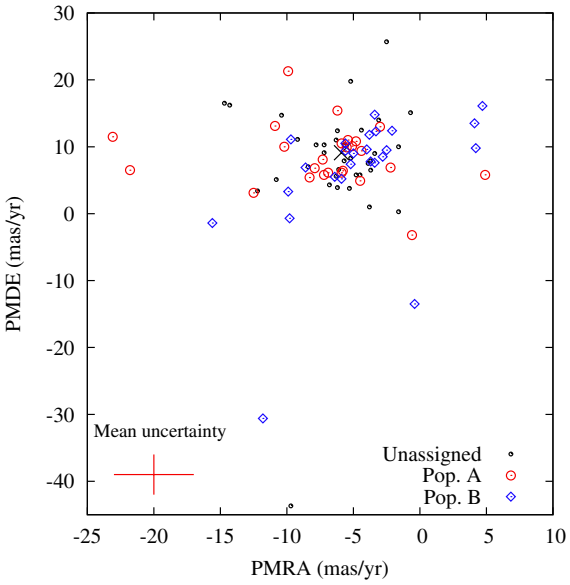

Fig. 14. UCAC4 proper motions (in milli-arcseconds per year) for our selected Gamma Vel members. The different symbols correspond to the various populations as described in Fig. 9. The proper motion of γ^2 Vel itself is shown with a cross. There are 6 objects that lie beyond the borders of the plot. These and the other very discrepant objects show evidence of binarity or lie very close to γ^2 Vel and are likely to have unreliable proper motions.

5. Discussion

The RV distribution of the young, low-mass stars surrounding γ^2 Vel clearly exhibits structure that has a bearing on the current dynamical state and the star formation history of the region. The evidence at hand can be summarised as follows.

- The RV distribution must be modelled with more than one component. A good fit is obtained by dividing the young stars into two, roughly equal, kinematic populations A and B, one with a narrow intrinsic dispersion ($\sigma_A = 0.34 \pm 0.16\,\mathrm{km\,s^{-1}}$) and the other much broader ($\sigma_B = 1.60 \pm 0.37\,\mathrm{km\,s^{-1}}$). The populations are significantly offset from each other by $2.15 \pm 0.48\,\mathrm{km\,s^{-1}}$.
- Pozzo et al. (2000) and J09 showed that the young, low-mass stars have a spatial density distribution that is concentrated towards γ^2 Vel. Here, we have shown that this concentration is mostly evident in population A, which has a centroid consistent with the position of γ^2 Vel. Population B appears less spatially concentrated and may be consistent with a uniform distribution across our surveyed area. The lack of a clean kinematic separation between the populations prevents us being more definitive.
- The two populations are not clearly distinguished from each other in the $V - I/V$ CMD or by their rotational properties. Their proper motions are similar and consistent with the proper motions of γ^2 Vel and the wider Vela OB2 association that extends well beyond the spatial extent of the GES data.
- The mid M-type objects in Population A do show significantly more Li depletion than those in Population B. This difference is robust to how the populations are separated kinematically and suggests that population A could be older on average by perhaps 1–2 Myr. The presence of stars that appear undepleted and depleted in both populations implies that their age distributions may overlap, though this latter conclusion is again weakened by the lack of clear kinematic separation of the populations.

We can hypothesize a number of scenarios for the origin of these two populations: (i) γ^2 Vel formed in an originally more massive, gas-rich cluster. Population A is the bound remnant of the cluster after gas expulsion and population B is an unbound halo of escaping stars. We refer to this as the "core-halo scenario"; (ii) γ^2 Vel formed in an isolated way but has attracted a retinue of low-mass stars from the dispersed Vela OB2 association. Population A would be the "captured" stars whilst population B is the dispersed low-mass component of Vela OB2. We refer to this as the "captured cluster" scenario; (iii) γ^2 Vel formed in a denser sub-clustering of the Vela OB2 association. At least part of this subcluster survived any gas expulsion to form population A, while population B consists of the dispersed low-mass component of the Vela OB2 association. We refer to this as the "cluster plus association" scenario. We consider each of these possibilities in turn with reference to the evidence listed above.

5.1. The core-halo scenario

It would be very rare for a star as massive as γ^2 Vel (with initial mass $\simeq 35\,M_\odot + 31.5\,M_\odot$; Eldridge 2009) to form in a cluster with total mass $\sim 100\,M_\odot$. The cluster would be the most distant outlier from the relationship between cluster mass and mass of the most massive star proposed by Weidner et al. (2010), where instead the expected *initial* cluster mass would be $\sim 1000\,M_\odot$. Gas expulsion might solve this problem (and is the reason that Weidner et al. excluded γ^2 Vel from their sample). The fraction of stars lost after gas expulsion depends on the (local) star forming efficiency, ratio of half-mass radius to tidal radius, how quickly the gas is lost and the initial clumpiness of the gas and stars (e.g. Gieles 2010; Bastian 2011). Many simulations show (e.g. Baumgardt & Kroupa 2007; Fellhauer et al. 2009; Moeckel & Bate 2011) that gas removal on less than a dynamical timescale or a low star formation efficiency can lead to the loss of most of the original cluster, leaving a bound remnant (Population A), that may be orders of magnitude less dense than the original embedded cluster, surrounded by an expanding halo (Population B).

The dynamics of this scenario can be checked using the velocity dispersions of the two populations. Clusters in virial equilibrium have RV dispersions (σ_v) that are related to their total dynamical masses ($M_{\rm dyn}$) and projected half mass radii (r_m) by

$$M_{\rm dyn} = \eta \frac{\sigma_v^2 r_m}{G}, \tag{5}$$

where η is a numerical constant related to the density profile and is approximately 10 for a Plummer density distribution (Spitzer 1987; Portegies Zwart et al. 2010).

If we sum up the Gamma Vel members in our survey, weighted according to their probability of belonging to population A, and assuming that those that lie outside $8 < RV < 26\,\mathrm{km\,s^{-1}}$ have $P_A = f_A = 0.48$, then the total mass of population A (among the GES survey objects) is $58\,M_\odot$. This mass estimate should be increased by a factor 1/0.85 to reflect that GES spectroscopy was obtained for 85 per cent of cluster candidates and by another factor of 1.25 to account for an assumed binary fraction of 0.46 with a flat mass ratio distribution between 0.1 and 1 (see Sect. 4.1). If we further assume that our survey covers the full extent of population A and that it is centred on γ^2 Vel, then the half mass radius of this distributed population is $r_m = 0.225$ degrees, equivalent to 1.37 pc at the distance of the cluster.

To these low-mass stars we can add the more massive stars that are not included in GES. These are obtained from the Tycho catalogue and filtered on proper motion and their position in the V versus $B-V$ CMD to obtain a list of secure association members (see J09). We assign masses to these based on their V magnitudes and a $Z = 0.02$ 10 Myr isochrone from the Siess et al. (2000) models. There are 13 stars which are likely association members and within the area surveyed by GES, with a total mass of 32 $M_{\odot}$. However, we do not know if these belong to populations A or B, so assign a fraction $f_{\rm A}$ of the mass to population A. The total mass of distributed stars in population A is therefore $(58 \times 1.25/0.85) + (32 \times 0.48) = 101\ M_{\odot}$, where we neglect the contribution of any stars below 0.2 $M_{\odot}$. We also neglect the contribution from any residual gas. The low and uniform extinction towards the early type stars of the Gamma Vel cluster suggests this is justified.

The central concentration of population A and the positional coincidence between its centroid and the position of γ^2 Vel, suggest that γ Vel belongs to population A. If so, the total mass of that system is 39 $M_{\odot}$ (for γ^2 Vel; de Marco & Schmutz 1999) and a further 12 $M_{\odot}$ for its proper motion companion γ^1 Vel, which is a resolved multiple with components for which we estimate masses of 7 $M_{\odot}$ and 5 $M_{\odot}$ respectively. The addition of this mass alone to the population A "cluster" would increase σ_v, but as it is all added to the centre, it also decreases η to $\simeq$6.3 and the final expected virial velocity from Eq. (5) is $\sigma_v = 0.28\,{\rm km\,s^{-1}}$ (or about $0.18\,{\rm km\,s^{-1}}$ if γ Vel were *not* part of population A). The measured RV dispersion is $\sigma_{\rm A} = 0.34 \pm 0.16\,{\rm km\,s^{-1}}$, so population A appears consistent with virial equilibrium and currently bound. If population B were also spatially centred on γ^2 Vel it would roughly double the total mass, but its velocity dispersion of $\sigma_{\rm B} = 1.60 \pm 0.37\,{\rm km\,s^{-1}}$ would clearly make it unbound.

Although this scenario is consistent with the velocity dispersions, there is no simple explanation for why population B would have a mean velocity that is significantly different to population A or why there should be a gradient in the mean RV of population B. It is also unclear why there would be any difference in the mean ages of the populations manifested as the differences seen in Li depletion. For these reasons we think this scenario is unlikely.

5.2. Captured cluster scenario

If γ^2 Vel formed as part of an initially supervirial OB association. Then, despite the global expansion, it may have captured a retinue of lower mass stars in its local potential well (e.g. Parker et al. 2014). In this scenario population A would be captured low-mass stars and population B would be expanding remnants of the original association. Stars in the original association would have a (supervirial) velocity dispersion, but the captured stars would settle into a new equilibrium roughly centred on the peculiar velocity of the γ Vel system. This might explain why the two populations have discrepant, but overlapping velocity distributions. The evolution of such a substructure within an expanding association could occur on a dynamical timescale $\simeq (GM_{\gamma\ {\rm Vel}}/r_m^3)^{-1/2}) \simeq 3$ Myr.

Given that γ^2 Vel has an age of $\geq$5 Myr (see below) there appears to be time for this process to have occurred. Furthermore, because the captured stars are most likely to have similar velocities to γ^2 Vel, this can explain the small velocity dispersion of population A. However, there is no simple explanation for any age or composition difference between the populations as suggested by the difference in photospheric Li among their M-dwarfs.

5.3. Cluster plus association scenario

A hybrid of these two models is that γ Vel formed near the centre of a locally dense region, whilst less dense regions formed stars with lower efficiency which became the wider Vela OB2 association (e.g. see the numerical simulations by Bonnell et al. 2011). Following gas expulsion, this dense region expanded and lost some fraction of its members. With an escape velocity of $\sim$1 km s^{-1}, this halo of lost stars has expanded to of order 5 pc radius and been diluted into the general background of objects in Vela OB2. Population A is then the bound remnant of the originally dense region and population B is mostly formed of a general background of young objects in the wider Vela OB2 association. If population A is older by 1–2 Myr, then the very small difference in the loci of the two populations in the CMD would mean that population A would need to be closer (on average) than B by about 10–20 pc. In such an extended region of star formation, it is hardly surprising that age differences of 1–2 Myr or RV differences of $\sim$2 km s^{-1} exist. A similar situation applies on similar scales in other star forming regions. Tobin et al. (2009) finds RV gradients of $\simeq$0.3 km s^{-1} pc^{-1} on $\simeq$10 pc scales in Orion A, very similar in magnitude to what is found here in population B.

The "cluster" defined by population A is barely bound. Its current crossing time of a few Myr is similar to the age of γ^2 Vel and so it falls on the cusp of the $t_{\rm cross}/{\rm age} \sim 1$ criterion that can be used to separate bound clusters from unbound associations (see Gieles & Portegies Zwart 2011), an outcome predicted by models that assume a reasonably high star forming efficiency ($\geq$30 per cent; Pelupessy & Portegies Zwart 2012). It seems unlikely that it will remain as a bound entity for very long. The tidal radius of the cluster in the gravitational field of the Galaxy, is approximately $r_{\rm t} \simeq 1.4(M/M_{\odot})^{1/3}$ at the solar Galactocentric radius, so $r_{\rm t}/r_m \simeq 5$. The relaxation time is only a few times the crossing time, so significant evaporation should take place on timescales of 10 Myr, and this will be exacerbated by the significant mass loss expected within the next few Myr from γ^2 Vel through winds and supernovae.

These first kinematic results for a young cluster in the *Gaia*-ESO survey demonstrate their power in deciphering the histories and predicting the futures of star forming regions. The RVs and kinematically unbiased membership determination offered by the GES data will be complementary to proper motions and parallaxes from the *Gaia* spacecraft. *Gaia* should give the distances to individual stars at the distance of γ^2 Vel (at $V \sim 16$) to about $\pm$3 pc, and tangential velocities to $<$0.2 km s^{-1} for stars with $V \leq 20$. Such precision will allow searches for radially anisotropic velocity distributions associated with rapid gas expulsion (e.g. Baumgardt & Kroupa 2007) and precisely test whether population A is indeed closer on average than population B.

5.4. Age puzzle

A lingering mystery is that the γ^2 Vel system appears to be younger than the cluster (population A) that surrounds it. This issue was extensively discussed in J09, but in brief it was claimed that the age of γ^2 Vel, citing work by North et al. (2007), was 3.5 Myr and that this was younger than the low-mass PMS population around it on the basis of (i) comparison with theoretical isochrones in the $V-I/V$ CMD; (ii) empirical comparison of the locus of PMS stars in the CMD with those in other star forming regions of known (or assumed to be known) age. These considerations along with the *lack* of Li depletion

among the G/K-type stars led to an age estimate of 5–10 Myr and to an inferred star forming history where the most massive object (γ^2 Vel) forms last in accordance with the "sorted sampling" hypothesis of Weidner & Kroupa (2006).

Using evolutionary models that incorporated binary interactions and rotation, Eldridge (2009) revised the age of γ^2 Vel upwards to 5.5 ± 1 Myr, weakening the case for any age discrepancy with the low-mass cluster. However it is now worth revisiting the age of the low-mass cluster too, because the new Li data we present here are more constraining and also because the overall age scale of young clusters, and in particular the ages of the clusters to which the Gamma Vel cluster was compared have been revised.

The absolute age determined by comparison to low-mass isochrones is unchanged with respect to the situation described in J09 and illustrated in their Fig. 13 and in Figs. 4 and 9 in this paper. The results are highly model dependent (models vary because of different assumptions about atmospheres, convective efficiency and opacities), and also depend on how luminosities and temperatures are converted into the observational plane, but currently suggest an age somewhere between 10 and 20 Myr.

In J09 (their Fig. 15), the empirical locus of the low-mass stars in the $V - I/V$ CMD was found to be older than that of σ Ori, λ Ori and NGC 2362, and similar to the 25 Ori cluster. The ages of the three younger clusters have been homogeneously reanalysed using their high-mass populations and revised upwards to 6, 10 and 12 Myr respectively by Bell et al. (2013). Less model-dependence and systematic error is expected from ages determined by stars on the upper part of the main-sequence. On the same age scale the low-mass stars in the Gamma Vel cluster would have empirical isochronal ages >10 Myr.

An older age for the low-mass stars is also consistent with the Li depletion seen among the M-dwarfs (Fig. 12). Ages from Li depletion are also quite model dependent, but the models of Baraffe et al. (1998) predict little depletion for ages less than about 10 Myr (and unlike the CMD isochrones this is independent of the assumed distance). Models with higher convective efficiency can deplete Li faster, but also predict the depletion to occur in somewhat warmer stars first. A full investigation of the Li depletion pattern and comparison with models is deferred to a subsequent GES paper (Franciosini et al., in prep.). An empirical comparison is also possible; for instance Dahm (2005) shows that stars with $V - I \sim 2.7$ in NGC 2362 (age 12 Myr; Bell et al. 2013) show no evidence for significant Li depletion, whereas the β Pic association (age 21 ± 4 Myr; Binks & Jeffries 2014) has many M-dwarfs where Li cannot be detected (Mentuch et al. 2008). Hence this comparison also suggests that population A is older than 10 Myr (but younger than 20 Myr).

This issue is yet to be resolved conclusively, mainly due to the uncertainties in estimating the absolute ages of low-mass stars and the model-dependence of isochrones in the CMD and of Li depletion. The evidence as it stands still suggests that γ^2 Vel formed in a clustered environment and is significantly younger, by at least a few Myr, than the bulk of the surrounding low-mass population. This is qualitatively in agreement with massive star formation scenarios involving competitive accretion and mergers (e.g. Bonnell & Bate 2005; Bonnell et al. 2011). Perhaps an alternative explanation that might be explored is whether additional mass transfer between the components of γ^2 Vel could make them appear younger or whether the system was initially a triple and the present Wolf-Rayet component is the rejuvenated remnant of a merged close binary (e.g. de Mink et al. 2013), although the small separation of the current components may make the latter unlikely.

6. Summary

One of the main goals of GES is to characterise the current dynamical state of young clusters and star forming regions and attempt to infer their histories and predict their futures. A key part of this task is to deliver precision RV for young stars. The work in Sect. 2.3.1 shows that in the best cases ($v \sin i < 30\,\mathrm{km\,s^{-1}}$ and $S/N > 30$) that GES RVs have uncertainties of $0.25\,\mathrm{km\,s^{-1}}$ for a single observation and that this is dominated by systematic uncertainties associated with instrumental calibration.

The excellent RV precision has enabled us to uncover significant velocity structure in the low-mass stars surrounding the massive binary system γ^2 Vel. The RV distribution is reasonably modelled with two Gaussian components (populations A and B) with roughly equal numbers in each, one with a very narrow intrinsic width of $0.34 \pm 0.16\,\mathrm{km\,s^{-1}}$ and the other much broader, with a dispersion of $1.60 \pm 0.37\,\mathrm{km\,s^{-1}}$ and offset by $2\,\mathrm{km\,s^{-1}}$ from the first component. We have searched for other differences in the two overlapping kinematic populations, finding that population A is probably more centrally concentrated around γ^2 Vel than population B, and is about 1–2 Myr older from the evidence of significantly more photospheric Li depletion among its mid M-type members.

The velocity dispersion and estimated mass of population A indicate that it is roughly in virial equilibrium, but only tenuously bound, thanks to a short relaxation time and a half-mass radius that is only five times smaller than its tidal radius in the Galactic potential. It seems likely that population A is the bound remnant of an initially larger cluster, formed in a denser region of the Vela OB2 association, that has been partially disrupted by gas expulsion. Population B consists of a scattered population of unbound stars born in less dense regions of Vela OB2. γ^2 Vel appears to be younger by at least a few Myr than the bulk of the low-mass population surrounding it, suggesting a formation scenario in which γ^2 Vel forms after the low-mass stars, possibly terminating star formation and expelling gas.

Acknowledgements. Based on data products from observations made with ESO Telescopes at the La Silla Paranal Observatory under programme ID 188.B-3002. The results presented here benefited from discussions in three *Gaia*-ESO workshops supported by the ESF (European Science Foundation) through the GREAT (*Gaia* Research for European Astronomy Training) Research Network Program (Science meetings 3855, 4127 and 4415) This work was partially supported by the *Gaia* Research for European Astronomy Training (GREAT-ITN) Marie Curie network, funded through the European Union Seventh Framework Programme [FP7/2007-2013] under grant agreement 264895 and supported by the European Union FP7 programme through ERC grant number 320360 and by the Leverhulme Trust through grant RPG-2012-541. We acknowledge the support from INAF and Ministero dell' Istruzione, dell' Università e della Ricerca (MIUR) in the form of the grant "Premiale VLT 2012". RJJ acknowledges financial support from the UK Science and Technology Facilities Council.

References

Baraffe, I., Chabrier, G., Allard, F., & Hauschildt, P. H. 1998, A&A, 337, 403
Bastian, N. 2011, in Proc. Stellar Clusters and Associations: A RIA Workshop on Gaia, 85
Baumgardt, H., & Kroupa, P. 2007, MNRAS, 380, 1589
Bell, C. P. M., Naylor, T., Mayne, N. J., Jeffries, R. D., & Littlefair, S. P. 2013, MNRAS, 434, 806
Binks, A. S., & Jeffries, R. D. 2014, MNRAS, 438, L11
Bonnell, I. A., & Bate, M. R. 2005, MNRAS, 362, 915
Bonnell, I. A., Smith, R. J., Clark, P. C., & Bate, M. R. 2011, MNRAS, 410, 2339
Bressert, E., Bastian, N., Gutermuth, R., et al. 2010, MNRAS, 409, L54
Briceño, C., Hartmann, L., Hernández, J., et al. 2007, ApJ, 661, 1119
Brown, J. A., Sneden, C., Lambert, D. L., & Dutchover, Jr., E. 1989, ApJS, 71, 293
Carpenter, J. M. 2000, AJ, 120, 3139

Cayrel, R. 1988, in The Impact of Very High S/N Spectroscopy on Stellar Physics, eds. G. Cayrel de Strobel, & M. Spite, IAU Symp., 132, 345
Clark, P. C., Bonnell, I. A., Zinnecker, H., & Bate, M. R. 2005, MNRAS, 359, 809
Cottaar, M., Meyer, M. R., Andersen, M., & Espinoza, P. 2012a, A&A, 539, A5
Cottaar, M., Meyer, M. R., & Parker, R. J. 2012b, A&A, 547, A35
Dahm, S. E. 2005, AJ, 130, 1805
De Marco, O., & Schmutz, W. 1999, A&A, 345, 163
de Mink, S. E., Sana, H., Langer, N., Izzard, R. G., & Schneider, F. R. N. 2013, ApJ, submitted [arXiv:1312.3650]
de Zeeuw, P. T., Hoogerwerf, R., de Bruijne, J. H. J., Brown, A. G. A., & Blaauw, A. 1999, AJ, 117, 354
Duchêne, G., & Kraus, A. 2013, ARA&A, 51, 269
Eldridge, J. J. 2009, MNRAS, 400, L20
Fellhauer, M., Wilkinson, M. I., & Kroupa, P. 2009, MNRAS, 397, 954
Fűrész, G., Hartmann, L. W., Szentgyorgyi, A. H., et al. 2006, ApJ, 648, 1090
Fűrész, G., Hartmann, L. W., Megeath, S. T., Szentgyorgyi, A. H., & Hamden, E. T. 2008, ApJ, 676, 1109
Gieles, M. 2010, in IAU Symp. 266, eds. R. de Grijs, & J. R. D. Lépine, 69
Gieles, M., & Portegies Zwart, S. F. 2011, MNRAS, 410, L6
Gilmore, G., Randich, S., Asplund, M., et al. 2012, The Messenger, 147, 25
Goodwin, S. P., & Bastian, N. 2006, MNRAS, 373, 752
Hernández, C. A., & Sahade, J. 1980, PASP, 92, 819
Hernández, J., Hartmann, L., Calvet, N., et al. 2008, ApJ, 686, 1195
Hills, J. G. 1980, ApJ, 235, 986
Horne, K. 1986, PASP, 98, 609
Jackson, R. J., & Jeffries, R. D. 2010, MNRAS, 407, 465
Jeffries, R. D., Oliveira, J. M., Barrado y Navascués, D., & Stauffer, J. R. 2003, MNRAS, 343, 1271
Jeffries, R. D., Maxted, P. F. L., Oliveira, J. M., & Naylor, T. 2006, MNRAS, 371, L6
Jeffries, R. D., Naylor, T., Walter, F. M., Pozzo, M. P., & Devey, C. R. 2009, MNRAS, 393, 538
Kroupa, P., Aarseth, S., & Hurley, J. 2001, MNRAS, 321, 699
Kruijssen, J. M. D., Maschberger, T., Moeckel, N., et al. 2012, MNRAS, 419, 841
Kurucz, R. 1993, ATLAS9 Stellar Atmosphere Programs and 2 km s^{-1} grid. Kurucz CD-ROM No. 13 (Cambridge, Mass.: Smithsonian Astrophysical Observatory)
Lada, C. J., & Lada, E. A. 2003, ARA&A, 41, 57
Maxted, P. F. L., Jeffries, R. D., Oliveira, J. M., Naylor, T., & Jackson, R. J. 2008, MNRAS, 385, 2210
Mentuch, E., Brandeker, A., van Kerkwijk, M. H., Jayawardhana, R., & Hauschildt, P. H. 2008, ApJ, 689, 1127
Millour, F., Petrov, R. G., Chesneau, O., et al. 2007, A&A, 464, 107
Munari, U., Sordo, R., Castelli, F., & Zwitter, T. 2005, A&A, 442, 1127
North, J. R., Tuthill, P. G., Tango, W. J., & Davis, J. 2007, MNRAS, 377, 415
Palla, F., Randich, S., Pavlenko, Y. V., Flaccomio, E., & Pallavicini, R. 2007, ApJ, 659, L41
Parker, R. J., Wright, N. J., Goodwin, S. P., & Meyer, M. R. 2014, MNRAS, 438, 620
Pasquini, L., Avila, G., Blecha, A., et al. 2002, The Messenger, 110, 1
Patten, B. M., & Simon, T. 1996, ApJS, 106, 489
Pelupessy, F. I. & Portegies Zwart, S. 2012, MNRAS, 420, 1503
Perryman, M. A. C., de Boer, K. S., Gilmore, G., et al. 2001, A&A, 369, 339
Piau, L., & Turck-Chièze, S. 2002, ApJ, 566, 419
Portegies Zwart, S. F., McMillan, S. L. W., & Gieles, M. 2010, ARA&A, 48, 431
Pozzo, M., Jeffries, R. D., Naylor, T., et al. 2000, MNRAS, 313, L23
Raghavan, D., McAlister, H. A., Henry, T. J., et al. 2010, ApJS, 190, 1
Randich, S., & Gilmore, G. 2013, The Messenger, 154, 47
Randich, S., Aharpour, N., Pallavicini, R., Prosser, C. F., & Stauffer, J. R. 1997, A&A, 323, 86
Randich, S., Pallavicini, R., Meola, G., Stauffer, J. R., & Balachandran, S. C. 2001, A&A, 372, 862
Sacco, G. G., Franciosini, E., Randich, S., & Pallavicini, R. 2008, A&A, 488, 167
Schaerer, D., Schmutz, W., & Grenon, M. 1997, ApJ, 484, L153
Siess, L., Dufour, E., & Forestini, M. 2000, A&A, 358, 593
Smith, L. F. 1968, MNRAS, 138, 109
Soderblom, D. R. 2010, ARA&A, 48, 581
Soderblom, D. R., Jones, B. F., Balachandran, S., et al. 1993, AJ, 106, 1059
Spitzer, L. 1987, Dynamical evolution of globular clusters (Princeton University Press)
Stetson, P. B., & Pancino, E. 2008, PASP, 120, 1332
Tobin, J. J., Hartmann, L., Furesz, G., Mateo, M., & Megeath, S. T. 2009, ApJ, 697, 1103
Tokovinin, A., Cantarutti, R., Tighe, R., et al. 2010, PASP, 122, 1483
Tutukov, A. V. 1978, A&A, 70, 57
van Leeuwen, F. 2007, A&A, 474, 653
Weidner, C., & Kroupa, P. 2006, MNRAS, 365, 1333
Weidner, C., Kroupa, P., & Bonnell, I. A. D. 2010, MNRAS, 401, 275
Zacharias, N., Finch, C. T., Girard, T. M., et al. 2013, AJ, 145, 44
Zapatero Osorio, M. R., Béjar, V. J. S., Pavlenko, Y., et al. 2002, A&A, 384, 937